JOURNAL OF GEOPHYSICAL RESEARCH, VOL. 112, E04S11, doi:10.1029/2006JE002874, 2007

Superrotation in a Venus general circulation model

C. Lee,[1,2] S. R. Lewis,[3] and P. L. Read[1]

Received 30 November 2006; revised 17 January 2007; accepted 1 February 2007; published 6 April 2007.

[1] A superrotating atmosphere with equatorial winds of $\sim$35 m s^{-1} is simulated using a simplified Venus general circulation model (GCM). The equatorial superrotation in the model atmosphere is maintained by barotropic instabilities in the midlatitude jets which transport angular momentum toward the equator. The midlatitude jets are maintained by the mean meridional circulation, and the momentum transporting waves are qualitatively similar to observed midlatitude waves; an equatorial Kelvin wave is also present in the atmosphere. The GCM is forced by linearized cooling and friction parameterizations, with hyperdiffusion and a polar Fourier filter to maintain numerical stability. Atmospheric superrotation is a robust feature of the model and is spontaneously produced without specific tuning. A strong meridional circulation develops in the form of a single Hadley cell, extending from the equator to the pole in both hemispheres, and from the surface to 50 km altitude. The zonal jets produced by this circulation reach 45 m s^{-1} at 60 km, with peak winds of 35 m s^{-1} at the equator. A warm pole and cold collar are also found in the GCM, caused by adiabatic warming in the mean meridional circulation. Wave frequencies and zonal wind speeds are smaller than in observations by cloud tracking but are consistent with a Doppler shifting by wind speeds in the generating region of each wave. Magnitudes of polar temperature anomalies are smaller than the observed features, suggesting dynamical processes alone may not be sufficient to maintain the large observed temperature contrasts at the magnitudes and periods found in this GCM.

Citation: Lee, C., S. R. Lewis, and P. L. Read (2007), Superrotation in a Venus general circulation model, *J. Geophys. Res.*, *112*, E04S11, doi:10.1029/2006JE002874.

1. Introduction

[2] Equatorial winds with a westward speed of 120 m s^{-1} are observed in the dayside cloud decks of the Venus atmosphere [*Lebonnois et al.*, 2006], more than 35 times faster than the surface rotation. Such a strong westward (prograde) wind cannot be maintained on the equator by the axisymmetric meridional circulation, because of its inability to maintain an extremum of angular momentum away from the boundary layer [*Hide*, 1969; *Schneider*, 2006]. In order to produce the observed wind speeds on the equator, a nonaxisymmetric process must exist in the atmosphere to transport the momentum toward the equatorial jet region.

[3] A number of atmospheric processes have been suggested to explain this momentum transport, often separated into two groups [e.g., *Seiff*, 1983; *Del Genio and Rossow*, 1990]. The first group of processes transport momentum horizontally from the midlatitudes (from the midlatitude jets) toward the equator. *Gierasch* [1975], for example, suggested horizontal transport by small scale viscous eddies or large scale thermal tides.

[4] The second group of processes transport momentum vertically into the jet region, usually from the lower atmosphere. For example, *Fels and Lindzen* [1974] and *Fels* [1977] suggested gravity waves could transport enough momentum toward the equator, driven either by direct thermal excitation or by orographic scattering of downward propagating waves. *Imamura* [2006] suggested the vertical wind shear might act to focus both the equatorial Kelvin wave and the midlatitude waves to accelerate the equatorial jet.

[5] In this study, we use the dynamical core of the Hadley Centre General Circulation Model [*Cullen*, 1993] with simplified parameterizations to provide the thermal forcing of the atmosphere and momentum dissipation in the boundary layer [*Lee et al.*, 2005]. Using this GCM we are able to reproduce a strong equatorial superrotation in the middle atmosphere, driven predominantly by planetary scale Rossby-like waves which transport (prograde) momentum horizontally toward the equator.

[6] In section 2 we describe the model parameterizations, and justify the quantitative values for each parameterization used in the model. In section 3 we examine the resulting zonal mean state of the atmosphere and the momentum transports, and we describe the processes which lead to the superrotation observed in this model. In section 4 we

[1]Department of Physics, University of Oxford, Oxford, UK.
[2]Now at Division of Geological and Planetary Sciences, California Institute of Technology, Pasadena, California, USA.
[3]Department of Physics and Astronomy, Open University, Milton Keynes, UK.

0148-0227/07/2006JE002874$09.00

Table 1. Vertical Levels Used in the GCM Described in Section 2 and $T_H(\eta)$ From Section 2 Which Specifies the Latitudinal Gradient of the Temperature Structure[a]

Level	η	T_H
0	9.602×10^{-1}	6.101
1	8.679×10^{-1}	6.136
2	7.577×10^{-1}	6.176
3	6.420×10^{-1}	6.410
4	5.299×10^{-1}	6.634
5	4.273×10^{-1}	6.678
6	3.373×10^{-1}	6.719
7	2.610×10^{-1}	6.762
8	1.979×10^{-1}	7.167
9	1.472×10^{-1}	7.524
10	1.074×10^{-1}	9.840
11	7.672×10^{-2}	14.948
12	5.361×10^{-2}	21.370
13	3.657×10^{-2}	28.746
14	2.430×10^{-2}	36.373
15	1.569×10^{-2}	43.315
16	9.814×10^{-3}	48.534
17	5.929×10^{-3}	51.175
18	3.454×10^{-3}	50.757
19	1.934×10^{-3}	47.342
20	1.043×10^{-3}	41.536
21	5.400×10^{-4}	34.295
22	2.710×10^{-4}	26.758
23	1.324×10^{-4}	19.807
24	6.355×10^{-5}	14.001
25	3.070×10^{-5}	9.599
26	1.525×10^{-5}	6.504
27	7.950×10^{-6}	4.439
28	4.500×10^{-6}	3.126
29	2.925×10^{-6}	2.370
30	2.265×10^{-6}	2.000

[a]Each integer level is the "full" model level where temperatures are specified in the GCM, and the corresponding η value of the vertical level. The "half" levels include the surface at $\eta = 1.0$ which are given as $\eta_{i+\frac{1}{2}} = (\eta_i + \eta_{i+1})/2.0$. The surface pressure is initialized at 9.2×10^6 Pa. The equivalent heating rate is given by $T_H(\eta) \times k_T$ (K/Earth day).

describe the temperature structures which appear in the polar region in this GCM, and in section 5 we compare the results from this experiment with the results from other recent, successful, GCMs. Finally in section 6 we give a summary of our results.

[7] Note that where timescales are given in "days," we mean an Earth day of 86400 S.I. seconds. One Venus year lasts 225 days.

2. Model Parameterizations

[8] The Venus General Circulation Model (GCM) uses the dynamical core of the Hadley Centre Unified Model [*Cullen*, 1993], which solves the nonhydrostatic primitive equations in three dimensions using an Arakawa B grid [*Arakawa and Lamb*, 1977] with a five degree resolution over the entire surface of the planet, and a hybrid $\sigma - P$ coordinate in the vertical, with a maximum spacing of 3.3 km. The vertical level is denoted by η, which is defined as

$$P_\star \eta = \sigma_k P_\star + P_k, \tag{1}$$

where σ_k defines the terrain following coordinate levels, and P_k defines the constant pressure levels, both values defined for each vertical level. $P_\star$ is the surface pressure defined at each surface grid point.

[9] Forcing and dissipation in the model are provided by a linearized forcing of the temperature field ("Newtonian cooling") toward a longitudinally symmetric state and a linearized dissipation ("Rayleigh friction") of the near-surface winds toward rest. The boundary layer friction is parameterized as

$$\frac{\partial \vec{v}}{\partial t} = \cdots - k_{\mathrm{vf}} \cdot \vec{v}, \tag{2}$$

where t is time, $\vec{v}$ is the horizontal velocity vector (u, v), k_{vf} is the coefficient of friction with a value of 1/25 day^{-1} on the lowest model layer and is zero for all other levels. An additional sponge layer is implemented in the model on the top three numerical levels, where the dissipation of the eddy horizontal velocity $\vec{v}' = (u', v')$ is given by

$$\frac{\partial \vec{v}}{\partial t} = -k_{\mathrm{ve}}(\eta) \cdot \vec{v}', \tag{3}$$

and k_{ve} is the coefficient of friction with a value of $\frac{1\times10^6}{\eta}$ day^{-1} in the top three levels, and is zero for all other levels.

[10] The thermal forcing in the GCM is parameterized as

$$\frac{\partial T}{\partial t} = \cdots - k_{\mathrm{T}}\left[T - T_{\mathrm{eq}}(\phi, \eta)\right], \tag{4}$$

where T is the kinetic temperature, $k_{\mathrm{T}} = 1/25$ day^{-1} is the coefficient of thermal relaxation. T_{eq} is the thermal relaxation profile, which is a function of latitude ϕ and the vertical level $\eta \simeq P/P\star$. T_{eq} can be further decomposed into a horizontal mean component (a function of) and a residual,

$$T_{\mathrm{eq}} = \sum_{i=0}^{5} T_z^{(i)} (\log_{10} \eta)^i + T_{\mathrm{H}}(\eta) \cos\phi \tag{5}$$

where the mean value $T_Z(\eta)$ is derived from Pioneer Venus probe data [*Seiff et al.*, 1980] and the Venus International Reference Atmosphere [*Kliore et al.*, 1992] data, smoothed to a fifth order polynomial in $\log_{10}(\eta)$ with coefficients $T_Z = \{733.4861,\ 301.2670,\ 47.2002,\ -5.0230,\ -2.3257,\ -0.1896\}$.

[11] The residual coefficient T_{H} is a function of η only and is multiplied by a cosine latitude function to provide a latitudinal gradient in the thermal relaxation field, where the η value for each level and values of T_{H} on each model level are given in Table 1. The global mean temperature profile is shown in Figure 1. The latitudinal-height structure of the heating is shown in Figure 2. This structure is based on results from radiative modeling [e.g., *Crisp*, 1986; *Pollack and Young*, 1975] with a peak-heating in the middle atmosphere, but the absolute magnitude is increased to account for the reduced relaxation timescale used in the model.

[12] In addition to these parameterizations, the acceleration due to gravity is $g = 8.87$ ms^{-2}, surface pressure is $p_0 = 9.2 \times 10^6$ Pa, angular velocity is $\Omega = -2.99 \times 10^{-7}$ s^{-1}, and the planetary radius is $a_v = 6.040 \times 10^6$ m [*Colin*,

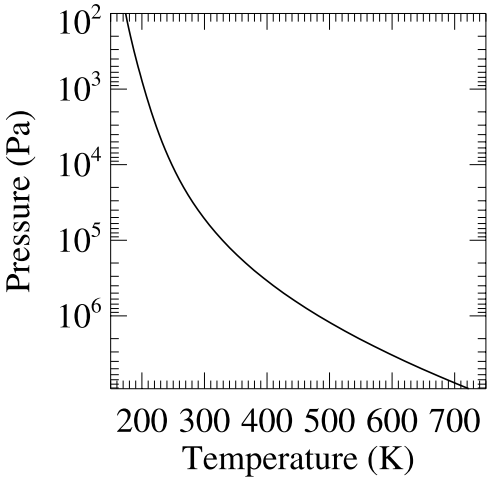

Figure 1. Global mean temperature profile used in the thermal relaxation profile in the GCM, as calculated from T_z in section 2.

1983]. Although the specific heat capacity of CO_2 is known to vary from 700 J kg^{-1} K^{-1} (at 200K) to 1150 J kg^{-1} K^{-1} (at 750K) [*Chase*, 1998], the specific heat capacity at constant pressure in this experiment is assumed to be constant with a value of c_p = 887 J kg^{-1} K^{-1}, its value at ~350 K.

[13] In the GCM the radiative heating is simulated by applying a height dependent latitudinal temperature gradient to the globally averaged temperature profile. Where the radiative heating is assumed to be largest, the latitudinal temperature gradient of equilibrium state is largest in the prescribed temperature field. Radiative modeling by *Crisp* [1986] and *Pollack and Young* [1975] suggest that most of the heating should occur in the cloud decks at 50 km, where 50% of the radiative heating is caused by absorption of ultraviolet radiation by an unknown species [*Kerzhanovich et al.*, 2003; *Esposito et al.*, 1983]. Only a small amount of radiation penetrates the cloud decks and is absorbed in the lower atmosphere, and the heating decreases below the cloud decks. Above the cloud decks the atmosphere is heated strongly by solar radiation, but the relaxation timescale of the atmosphere is relatively short in this region.

[14] In the GCM the latitudinal temperature gradient (Figure 2) applied to the global equilibrium temperature profile (Figure 1) peaks at 45–50 km altitude, and decreases to a small, finite value at the surface to reflect the small amount of heating that occurs there. Above the cloud decks the latitudinal temperature gradient decreases to zero, to model the short relaxation timescales of the atmosphere [*Pollack and Young*, 1975], and because of a numerical constraint of reducing any unwanted rigid lid effects on the GCM circulation.

[15] The prescribed heating in the lower atmosphere is highly idealized compared to the state of the Venus atmosphere derived from radiative models [*Crisp*, 1986; *Pollack and Young*, 1975]. In particular the radiative heating in the lower atmosphere is larger than is predicted by radiative transfer models. The reason for this modification is that we use a short (constant) relaxation timescale throughout the entire atmosphere to allow faster "spin-up" of the GCM, and the effective heating rate in the parameterization is dependent on this timescale as

$$\delta q \propto \frac{\delta T}{\tau}, \tag{6}$$

where τ is the relaxation timescale and δq is the specific heating rate. However, even with this simplified heating, the GCM does spontaneously produce superrotating winds (as do the *Yamamoto and Takahashi* [2003a] and *Herrnstein and Dowling* [2007] GCMs). Moreover, the wave activity which is present in the model atmosphere is qualitatively similar to the observed waves on Venus from Pioneer Venus cloud tracking [*Del Genio and Rossow*, 1990].

[16] In addition to the Newtonian cooling and Rayleigh friction prescribed in the model, a conservative sixth-order horizontal numerical hyperdiffusion is used on all vertical levels, with a coefficient of $K_H = 1.0 \times 10^9$ m^{2}s$^{-\frac{1}{3}}$, corresponding to an e-folding time of 30 Earth days for the highest wave number modes. The Courant-Friedrichs-Lewy (CFL) criterion is used to define a conservative polar filter to maintain stability as the model domain converges. Both the numerical diffusion and the CFL filtering are standard features of the dynamical core of the Hadley Centre GCM. No explicit vertical diffusion is used in the GCM.

[17] To isolate the processes responsible for the momentum transports the GCM is kept as simple as possible. A flat topography is used and there is no diurnal variation or seasonal variation in the forcing or dissipation, and no chemical or latent heat effects are considered. The thermal relaxation field used in the GCM is convectively stable, but convection can occur if the atmosphere becomes statically unstable.

3. Results

[18] The experiment described here was started from a rest state with the global mean temperature profile (T_Z from section 2) and integrated for 100 years to allow the model to reach a statistically steady state. Figure 3 shows the globally

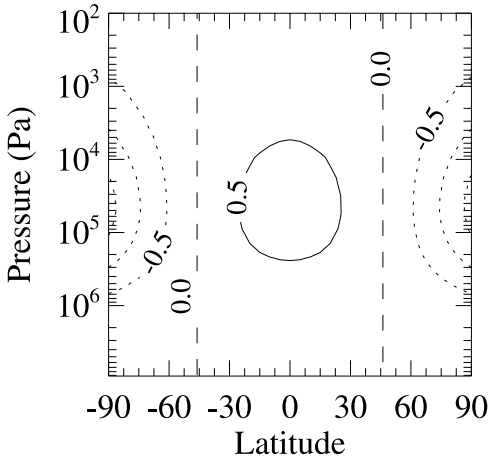

Figure 2. Latitude-height cross section of the deviation of the prescribed thermal relaxation field from the global mean in Figure 1. Calculated from $T_H(\eta)\cos\phi$ in section 2 and Table 1.

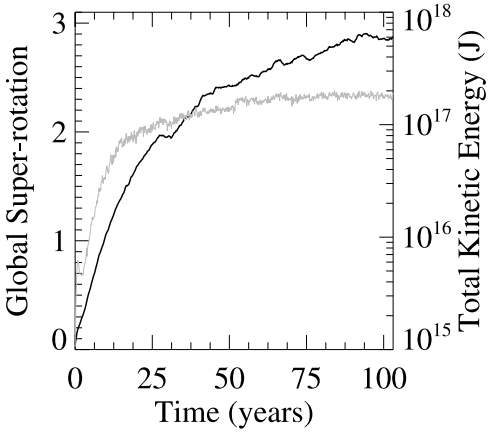

Figure 3. Globally integrated superrotation (black) as defined by *Read* [1986], and globally total integrated kinetic energy (gray), during the 100 year model integration. Diagnostics calculated from this GCM were taken over a 3 year period at the end of the 100 year integration.

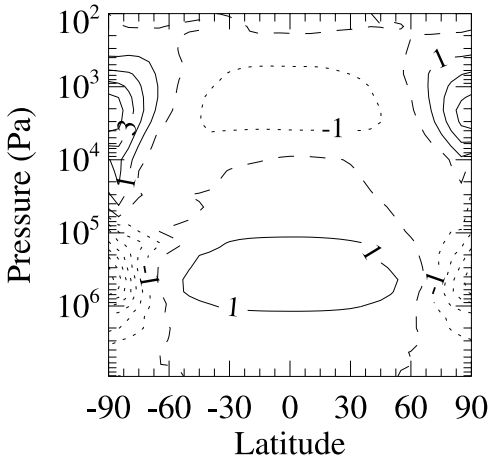

Figure 5. Latitude-height cross section of the anomaly temperature field, defined as $T'' = T - \overline{\overline{T}}$, where $\overline{\overline{T}}$ is the latitude and longitude mean of T, averaged over 3 years after 100 years. Δ = 1 K.

integrated kinetic energy and superrotation index for this experiment. In the last decade of the integration, the integrated kinetic energy of the zonal flow is still increasing, but by less than 0.15% per Venus year, and the mean growth rate over the last 30 years is 0.4% per Venus year. Without a sudden increase in the acceleration of the mean zonal flow, doubling the integration time would result in an increase of the integrated angular momentum of less than 15%. At the end of the 100 year integration diagnostics were calculated over a further 3 year period.

[19] Figure 4 shows the mean meridional mass stream function during the diagnostic period, defined as

$$\psi_m(\lambda, P) = \frac{2\pi a \cos\phi}{g} \int_0^{P'} \left[\overline{v(\lambda, P)}\right] dP, \tag{7}$$

where a is the planetary radius, ϕ is the latitude, g is the gravitational acceleration, P is the pressure, and v is the meridional wind. The stream function shows the mean meridional circulation extending from the equatorial surface to the polar region at 60 km, and a smaller indirect cell above this main overturning circulation. The latitudinal temperature gradients during the same period are shown in Figure 5 as the horizontal anomaly from the global mean temperature (i.e., $T - \overline{\overline{T}}$, where $\overline{\overline{T}}$ is the mean value of T in longitude and latitude). The zonal and time mean westward wind speed is shown in Figure 6, showing that the midlatitude jets forming near the downwelling region of the mean meridional circulation.

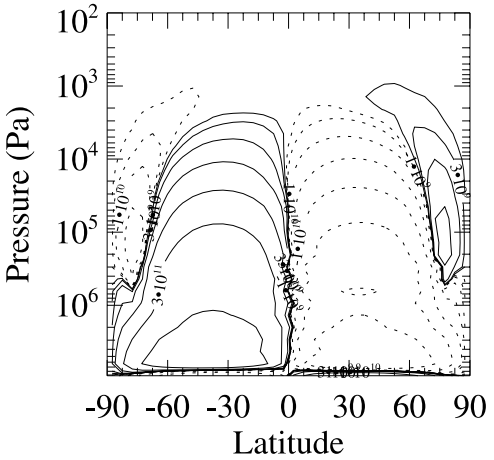

Figure 4. Latitude-height cross section of the meridional mass stream function derived from the global mean meridional wind field, averaged over 3 years after 100 years. As given in equation (7). Each contour level is 3 times larger than the preceding contour.

[20] In the equatorial region of the model, the mean zonal winds are westward (i.e., prograde, or superrotating) and are 20 times faster than the equatorial surface speed ($v_s = \Omega/a_v$). The globally integrated superrotation (as defined by *Read* [1986]) is $S \simeq 3$, suggesting the atmosphere contains 4 times the absolute angular momentum it would have at rest with respect to the planet surface. In comparison, $S \approx 0.05$ for Mars [*Lewis and Read*, 2003], which depends strongly on the dust loading of the atmosphere, while $S \approx 0.015$ for Earth [*Read*, 1986].

[21] The midlatitude jets are maintained by the mean meridional circulation in the atmosphere, which transports angular momentum in a single direct overturning circulation (e.g., the Hadley cell on Earth) from the surface to the middle atmosphere, and from the equator almost to the pole. The GCM does not reproduce the "stacked Hadley cells" structure that has been proposed to exist in the Venus atmosphere [e.g., *Schubert*, 1983].

[22] The equatorial superrotation must be maintained by a nonaxisymmetric process which transports net angular momentum into the equatorial region [*Hide*, 1969]. The angular momentum in the atmosphere can be accelerated by three different mechanisms, the axisymmetric circulation, the resolved eddy transport of momentum, and (particularly in a GCM) the unresolved eddies. From [*Read*, 1986] these terms can be expressed as

$$\overline{m}_t + \overline{\mathbf{u}}_\star \cdot \nabla \overline{m} = -\nabla \cdot \mathbf{E} + F/\rho. \tag{8}$$

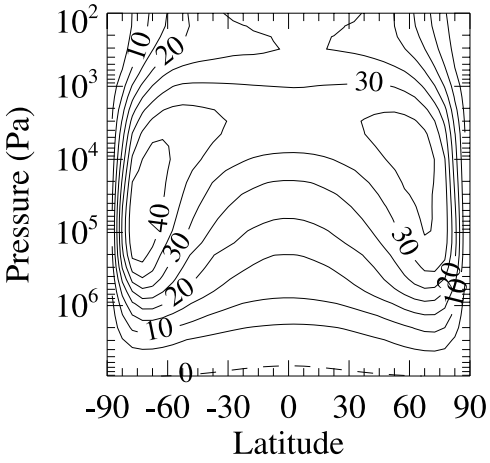

Figure 6. Latitude-height cross section of the zonal mean westward wind speed, averaged from 3 years of data at 100 years, $\Delta = 5$ m s^{-1}.

Where the first term ($\overline{m}_t$) is the acceleration of the specific angular momentum, where m is the specific angular momentum. The second term ($+\overline{\mathbf{u}}_\star \cdot \nabla \overline{m}$) is the deceleration of m caused by the Transformed Eulerian Mean circulation [*Andrews et al.*, 1987]. The third term ($-\nabla \cdot \mathbf{E}$) is the acceleration of m due to the nonaxisymmetric (wave/eddy) components via the divergence of the Eliassen-Palm flux **E**. Note that in this equation the Eliassen-Palm flux [*Eliassen and Palm*, 1961] **E** is expressed in terms of momentum transport, such that a convergence of the EP flux results in acceleration, this formulation uses the opposite sign convention to the formulation used to discuss "wave activity" [*Andrews et al.*, 1987]. The fourth term ($+F/\rho$) is the acceleration of m due to unresolved components in the GCM, such as the diffusion and filtering that are necessary to maintain numerical stability. Each term in equation (8) is described by *Read* [1986].

[23] An expanded formulation of this equation is given by *Zhu* [2006], where the author explicitly decomposes each term in equation (8) and calculates approximate values for the acceleration by a number of wave and mean circulation components.

[24] The time and longitudinal average of the four terms in equation (8) are shown in Figures 7 and 8, where the fourth term in equation (8) is calculated as the residual of the other terms, which are explicitly calculated from the model diagnostic fields. The midlatitude jets in the GCM are maintained by the mean overturning circulation (the second term in equation (8)), with the peak acceleration located near the downwelling branch of the circulation. In agreement with Hide's theorem [*Hide*, 1969] the axisymmetric circulation does not accelerate the equatorial jet.

[25] The numerical diffusion, shown in Figure 8, tends to *decelerate* the equatorial jet and the midlatitude jets (by a smaller amount). As a result the acceleration of the equatorial jet by the eddies is balanced by the mean meridional circulation and the numerical diffusion.

[26] The acceleration caused by the eddies is balanced predominantly by the mean circulation except on the equatorward side of the jet peaks, where the diffusion tends to be strongest. In the equatorial region, the explicitly resolved eddies/waves accelerate the mean westward winds, as is required to produce a superrotating jet on the equator.

[27] The acceleration by the eddies can be separated into the horizontal and vertical contributions (corresponding to the horizontal and vertical components of the EP flux divergence), these are shown in Figure 9 and Figure 10. The horizontal fluxes contribute to the net acceleration of the equatorial jet with a magnitude of

$$\frac{-\partial E_\phi}{\partial \phi} \approx \frac{dm}{dt} \approx 10 \text{ m}^2 \text{ s}^{-2}, \tag{9}$$

but the vertical EP fluxes do not accelerate the equatorial jet. Instead, the acceleration due to the horizontal fluxes are balanced by the mean meridional overturning and the unresolved components in the GCM. Reducing the numerical diffusion in this experiment by 30% tends to increase the equatorial jet by 5 m s^{-1} with the same globally integrated angular momentum.

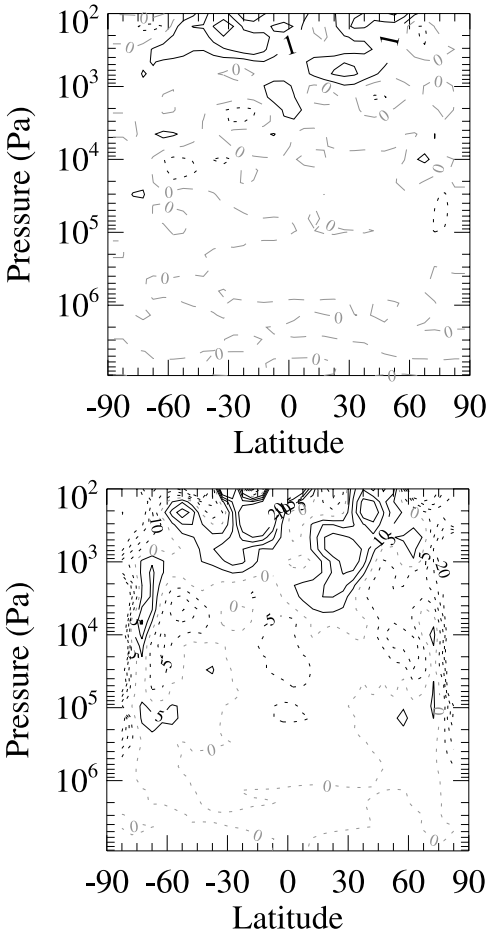

Figure 7. Individual terms in equation (8). Solid contours represent *acceleration* in each figure (regardless of sign), dotted contours represent *deceleration*, and the gray dashed contour is the zero contour. (top) Net acceleration of the zonal mean angular momentum ($\overline{m}_t$), $\Delta = 1$ m^2 s^{-2}. (bottom) Acceleration of $\overline{m}$ by the unresolved components in equation (8), calculated as the residual of the three preceding terms + F/ρ, $\Delta = 5$ m^2 s^{-2}. Figure 8 shows the TEM and Eliassen-Palm components.

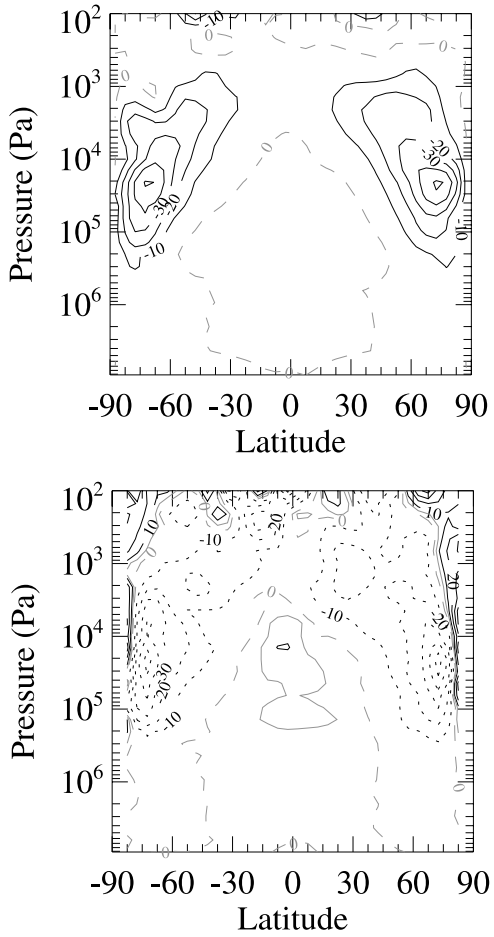

Figure 8. As Figure 7. (top) Deceleration of $\overline{m}$ by the mean circulation ($\overline{\mathbf{u}_\star} \cdot \nabla \overline{m}$), Δ = 10 m^2 s^{-2}. (bottom) Acceleration of the $\overline{m}$ by the resolved eddy components ($-\nabla \cdot \mathbf{E}$), Δ = 10 m^2 s^{-2}, the gray solid line is +5 m^2 s^{-2}.

[28] On the equatorward side of the jet region both horizontal and vertical contributions decelerate the midlatitude jet, while the horizontal EP fluxes tend to accelerate the poleward side of the jet above the jet region, balanced in part by a deceleration due to the vertical EP fluxes.

[29] The equatorward momentum transport in this experiment is dominated by the eddies in the midlatitudes, which in turn are dominated by a planetary wave number 1 mode with a period of 30 Earth days at 100 kPa. Figure 11 and Figure 12 show the periodograms for temperature and northward wind at a polar latitude (60N) and on the equator for this mode. The midlatitudes and poles of the GCM are dominated by the MRG-like mode (mixed Rossby-gravity) with components in wind and temperature. The dominant period of this wave is 30 Earth days near 100 kPa but has significant activity at longer periods in the lower atmosphere. The period of the waves in the lower atmosphere appears to be fixed relative to the mean flow at this latitude, as the period of the waves increases at approximately the same rate as the equivalent period of the mean flow with increasing atmospheric pressure.

[30] We identify this mode as a MRG-like mode because of the retrograde motion relative to the background winds

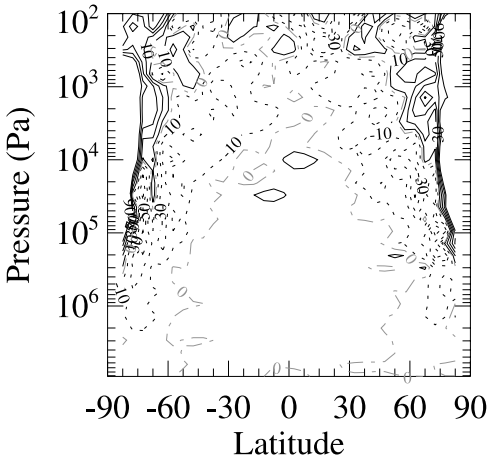

Figure 9. Horizontal divergence of the Eliassen-Palm vector, giving the acceleration of the zonal mean angular momentum by the horizontal eddy fluxes. Δ = 20 m^2 s^{-2} with the zero contour marked in gray.

[*Lindzen*, 1990], a positive correlation between v and T and a nonzero minimum near the equator [*Andrews et al.*, 1987].

[31] The structure of the MRG wave amplitude in latitude-pressure (not shown) corresponds closely to the Eliassen-Palm flux divergence shown in Figure 7, and the predominantly horizontal propagation of this wave agrees with the decomposition of the EP flux which has a larger horizontal component than the vertical component in the midlatitudes. The phase slope of the MRG wave with height itself varies with height and tends to become shallower in (and above) the jet region, with a corresponding increase in period, indicating a transfer of retrograde angular momentum from the wave into the mean zonal winds as the wave is dissipated [*Andrews et al.*, 1987]. The peak amplitude of the MRG wave occurs in a barotropically unstable region in the midlatitude jets near the westward jet peak, which is identified by an extremum in the second derivative of the westward wind speed with respect to latitude. That is, $\frac{\partial^2 \overline{u}}{\partial \phi^2} <$

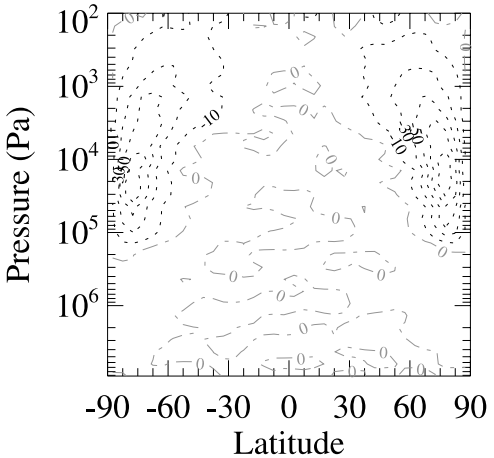

Figure 10. Vertical divergence of the Eliassen-Palm vector, giving the acceleration of the zonal mean angular momentum by the vertical eddy fluxes. Δ = 20 m^2 s^{-2} with the zero contour marked in gray.

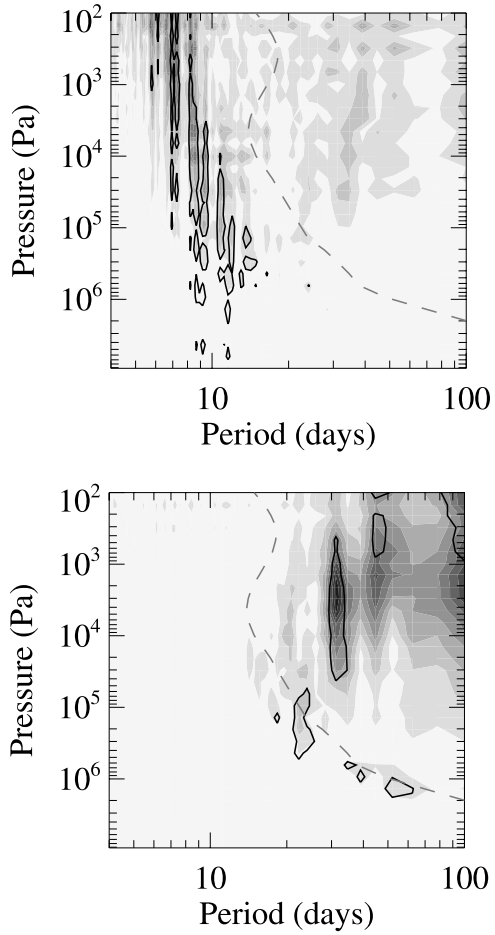

Figure 11. Periodogram of the waves in temperature (top) and northward wind at 60N. The dashed line on each plot is the time and longitude mean eastward wind, given in units of "equivalent period" (i.e., $\tau = 2\pi \cos \phi / a_v$) in Earth days. The sampling rate is 1/day, resulting in a Nyquist sampling limit of 2 days. The background shading on each plot is the wave amplitude at each pressure (Pa) and period (days); for temperature the amplitude range is 0 K-1 K (light-dark) in steps of 0.1 K, and for northward wind the amplitude range is 0 m s^{-1}–6 m s^{-1} in steps of 0.6 m s^{-1}. The solid black line-contour gives the 95% confidence level described in Appendix A.

$R\frac{\partial f}{\partial \phi}$, where f is the Coriolis parameter, R is radius, and ϕ is latitude [*Pedlosky*, 1987].

[32] The atmospheric fields in the equatorial region also have a contribution from the MRG-like wave, visible in the northward wind field of Figure 11 and Figure 12. In the temperature field (and the eastward wind field), an additional wave mode is found with a period of approximately 9 Earth days at 100 kPa, centered on the equator and with an amplitude which increases with height but decreases away from the equator. The lack of a significant signal in the northward wind field and the equatorial confinement of the wave suggest that this mode is a Kelvin wave. Both of these wave modes have been identified in cloud observations by Pioneer Venus [*Del Genio and Rossow*, 1990]. In this experiment, the period of the Kelvin mode is 9 ± 1 Earth days in the middle atmosphere. The latitude-pressure structure of the 9 day Kelvin wave indicates the growing amplitude of the Kelvin wave with decreasing pressure.

[33] Any acceleration of the equatorial jet caused by the Kelvin mode would most likely be present in the contribution of the vertical component of **E** to the EP flux divergence ($\nabla \cdot \mathbf{E}$). But this contribution is negligible compared to the contribution to $\nabla \cdot \mathbf{E}$ from the horizontal component of **E**. The Kelvin mode does not therefore appear to contribute significantly to the momentum transport in the GCM.

[34] The slope of the phase surface of the Kelvin mode (in longitude-height) changes sign at 100 kPa, such that at altitudes above this level the slope is westward with *increasing* height (on a westward rotating planet), and below this the slope is westward with *decreasing* height. The ageostrophic dispersion relation for the Kelvin wave [*Andrews et al.*, 1987] gives the relationship between the slope of the Kelvin wave and its direction of vertical propagation as

$$\frac{\partial z}{\partial x} = \frac{k_x}{k_z}, \tag{10}$$

where k_x and k_z are the horizontal and vertical wave number of the mode. An upward (downward) propagating Kelvin

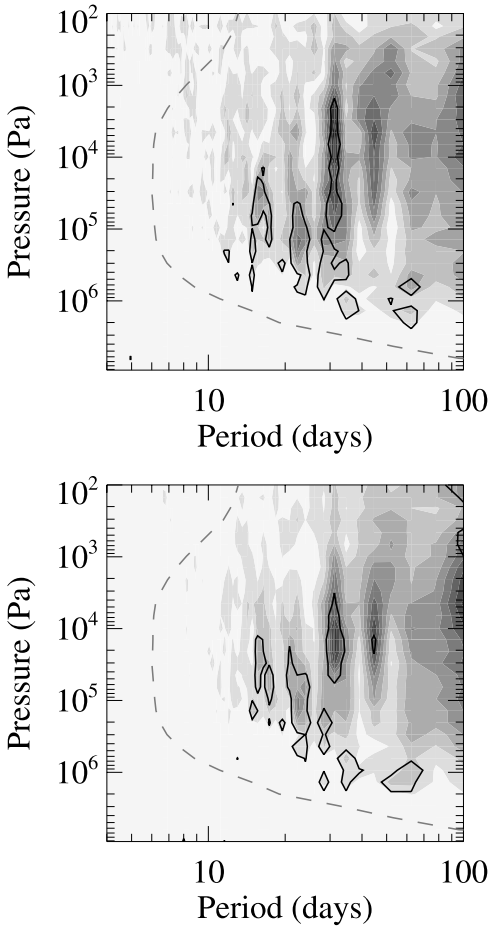

Figure 12. As Figure 11, on the equator.

wave has a westward slope on Venus with increasing (decreasing) height.

[35] The equatorial Kelvin wave in this GCM propagates away from its apparent source located between 500 kPa and 100 kPa. The downward propagating Kelvin wave has a weaker temperature signal as it propagates into a region of increasingly dense atmosphere, but is found to have a slightly longer period (11 ± 2.5 days) than the upward propagating wave.

[36] The layer of atmosphere between 500 kPa and 100 kPa (within 30 degrees of the equator) is inertially unstable for more than 50% of the 3 year sample analyzed and is a likely source of the Kelvin waves in the GCM atmosphere. In the Earth's atmosphere, inertial instability is found to induce wave activity near the equator [*Hayashi et al.*, 2002]. For Venus-like conditions, *Iga and Matsuda* [2005] analyze the effect of latitudinal shear of westward wind on the stability in the lower atmosphere and find that in an inertially stable circulation a shear instability can generate growing Kelvin modes, suggesting that the inertial instability found in this experiment is not the only possible source of the observed Kelvin mode.

4. Polar Structure

[37] The latitudinal temperature structure in Figure 5 shows a number of features which have been observed in the polar temperature fields on Venus [*Taylor et al.*, 1983]. In the lower atmosphere, the latitudinal temperature gradient is negative (positive) in the northern (southern) hemisphere, which is related to the direct meridional circulation in this region. Below 100 kPa the polar region is colder than the equator at all pressures (in the mean fields). In the upper atmosphere (at about 1 kPa), the latitudinal gradient is inverted so that the gradient is positive (negative) in the northern (southern) hemisphere. Between 10 kPa and 1 kPa the atmosphere poleward of 60 degrees is typically warmer than the equatorial region.

[38] This effect has been observed by the Pioneer Venus OIR instrument [*Taylor et al.*, 1983] and is referred to as the "warm pole." The region between 100 kPa and 10 kPa is a transition region between the two extremes, and has a relatively warm pole and equator, resulting in a band of relatively cold air surrounding the pole at 60 degrees in both hemispheres. This feature has also been observed by the OIR instrument and is referred to as the "cold collar." The "warm pole" feature is associated with the vertical shear of the jets through the cyclostrophic thermal wind balance [*Walterscheid et al.*, 1985],

$$2u\frac{\partial u}{\partial \zeta} = -\frac{R}{\tan\phi}\left(\frac{\partial T}{\partial \phi}\right)_P, \tag{11}$$

where $\zeta = -\ln\left(\frac{P}{P_0}\right)$, ϕ is latitude, and R is the specific gas constant of the Venus atmosphere. An increasing westward zonal jet speed with altitude (ζ) corresponds to a negative (positive) latitudinal temperature gradient in the northern (southern) hemisphere, and vice versa. The warm pole is thus related to the closing of the westward jet near 1 kPa. The cold collar in the GCM is present in the transition region between these two regimes and is correlated with the peak westward winds at each latitude. These features are also familiar in the atmospheres of Earth and Mars [e.g., *Read and Lewis*, 2004].

[39] The magnitudes of the "warm pole" and "cold collar" in the GCM (8K and 4K, respectively) are lower than in the observations (15K and 40K, respectively) so it is likely that the model is missing a dominant feedback mechanism in the polar region (e.g., a thermochemical feedback related to the lowering of cloud and hot dipole in the polar regions [*Esposito et al.*, 1983]) but it does suggest a possible mechanism which may contribute to the structure of the polar temperature structures. It is possible that increasing the horizontal resolution of the GCM will allow larger latitudinal gradients to exist in the atmosphere and increase the mean westward wind speed in the jets. For example, the *Yamamoto and Takahashi* [2003b] model uses the same GCM core as the *Yamamoto and Takahashi* [2003a] model but with a higher resolution, and the authors report a ~20% increase in the peak westward jet speed, although this may not be exclusively attributable to the increase in horizontal resolution.

5. Comparison With Recent Venus GCMs

[40] A number of GCMs have been successfully applied to the atmosphere of Venus recently. For example, the GCMs of *Yamamoto and Takahashi* [2003a] and *Herrnstein and Dowling* [2007] both achieve a significant equatorial superrotation using similar parameterizations for the radiative forcing of the atmosphere. In particular the *Yamamoto and Takahashi* [2003a] GCM reproduces a midlatitude jet of 100 m s^{-1}, with substantial equatorial superrotation and wave activity with period of 5–7 days.

[41] The GCM presented here and the *Yamamoto and Takahashi* [2003a] GCM both maintain a superrotation by a similar mechanism. A single meridional overturning cell extends from the surface to the jet region, providing the angular momentum necessary to maintain the midlatitude jet. Instabilities in the midlatitude jets generate planetary scale waves which transport angular momentum from these midlatitude jets toward the equator, where they maintain a strong superrotating flow. In the *Yamamoto and Takahashi* [2003a] GCM the midlatitude wave is a Rossby-like wave, with a period of 7.1 days.

[42] In the equatorial region, we find a Kelvin mode in agreement with the cloud tracking observations [*Del Genio and Rossow*, 1990], in contrast to *Yamamoto and Takahashi* [2003a], who find high wave number gravity waves (a planetary wave number of 4 or more). In a higher resolution (T21) version of the GCM, *Yamamoto and Takahashi* [2003b] identify a Kelvin wave with a period of 3–5 days and an inertially unstable lower atmosphere near the equator, as we report here. Neither of these GCMs suggest that the equatorial waves are significant in maintaining the equatorial superrotation.

[43] *Herrnstein and Dowling* [2007] find that topography affects the mean circulation and eddies in the atmosphere. In particular, the midlatitude jets become asymmetric with a slower jet in the northern hemisphere. Preliminary experiments with the topography in our GCM produce a much smaller change in the midlatitude jets (5 m s^{-1} compared to 20 m s^{-1} in the *Herrnstein and Dowling* [2007] GCM), and

the northern hemisphere jet is stronger than the southern hemisphere jet.

6. Summary and Conclusions

[44] The atmospheric circulation in this GCM shows a number of characteristic features of the Venus atmosphere, such as the midlatitude jets and equatorial superrotation, the MRG/Rossby-like midlatitude wave and the equatorial Kelvin wave, and qualitative analogs the polar temperature structures.

[45] The midlatitude jets are maintained by a single meridional overturning (Hadley-like) cell in each hemisphere, with peak westward wind speeds of 45 m s^{-1}, which are about half the magnitude measured by Pioneer Venus [e.g., *Seiff*, 1983]. It is not clear why the winds are much slower in this GCM experiment than in observations, but given the simplifications made in the linearized heating parameterization it is unlikely that the exact quantitative winds would be reproduced in the GCM. Further tuning of the heating parameterization tends to alter the jet structure and local superrotation in the GCM, but does not appear to change the global superrotation significantly.

[46] An equatorial superrotation is found in the GCM simulated atmosphere with peak westward winds of 30 m s^{-1} (about 20 times faster than the underlying surface, relative to an inertial rest frame). This superrotation is maintained by the planetary scale MRG/Rossby-like wave which transports momentum from the midlatitude jets to the equator.

[47] The MRG wave in the GCM is found to have a period of 30 ± 2 days, much slower than the ≈5 day period for the observed waves in the Venus cloud decks [*Del Genio and Rossow*, 1990]. A similar difference in period is found in the equatorial Kelvin wave, which is 9 ± 1 days in the model compared to ≈4 days in the observations.

[48] This difference in wave propagation speeds may be explained by a Doppler shift of the wave and wind speeds in the model to match the observations. Figure 11 and Figure 12 show that the wave periods are related to the zonal wind speeds, which supports this hypothesis. The *Yamamoto and Takahashi* [2003a] GCM, which has a 100 m s^{-1} equatorial jet, has correspondingly faster midlatitude and equatorial waves with periods of about 7 days.

Appendix A: Fourier Transform Significance Levels

[49] The significance levels in Figures 11 and 12 are calculated using a lag-1 autoregressive, AR(1), red noise process [*Allen and Smith*, 1996; *Torrence and Compo*, 1998]. The power spectrum of an AR(1) process is given by

$$P_k = \frac{1-\alpha^2}{1+\alpha^2-2\alpha\cos(2\pi k/N)}, \tag{A1}$$

where α is the lag-1 autocorrelation value, N is the number of points in the sample, k is the frequency index. The 95% confidence level for the power spectrum of the AR(1) process then calculated as

$$C_{95} = \frac{1}{2} P_k \chi_2^2 \sigma^2, \tag{A2}$$

where σ^2 is the variance of the data, χ_2^2 is the chi-square value for a process with two degrees of freedom (because we use a complex Fourier transform). To produce Figure 11 and Figure 12 the lag-1 autocorrelation, α, is calculated for each pressure and latitude and used to generate the AR(1) power spectrum. Amplitudes in the power spectrum which are above the 95% confidence level for the AR(1) process are considered significant at the 5% level. Care should be taken in interpreting the fine structure along the period axis, however, such as in the equatorial temperature periodogram (Figure 11, top), as these features are a result of the power spectrum having single frequency points above the confidence level. These narrow features can be sensitive to the sampling rate and tend to become broader in period with higher sampling rates.

[50] **Acknowledgments.** This work was undertaken as part of a DPhil. at the University of Oxford funded by the Particle Physics and Astronomy Research Council (PPARC). Funding to allow this work to be presented at the "Chapman Conference on Exploring Venus as a Terrestrial Planet" was provided in part by the European Space Agency (ESA) and the Royal Meteorological Society. We thank the two anonymous reviewers, whose comments helped improve this manuscript.

References

Allen, M. R., and L. A. Smith (1996), Monte Carlo SSA: Detecting irregular oscillations in the presence of colored noise, *J. Clim.*, *9*, 3373–3404.

Andrews, D. G., J. R. Holton, and C. B. Leovy (1987), *Middle Atmosphere Dynamics*, Elsevier, New York.

Arakawa, A., and V. R. Lamb (1977), Computational design of the basic dynamical processes of the UCLA General Circulation Model, *Methods Comput. Phys.*, *17*, 173–265.

Chase, M. W., Jr. (1998), *NIST-JANAF Thermochemical Tables*, 4th ed., *J. Phys. Chem. Ref. Data Monogr., 9*, 1-1951.

Colin, L. (1983), Basic facts about Venus, in *Venus*, edited by D. M. Hunten et al., pp. 10-26, Univ. of Ariz. Press, Tucson.

Crisp, D. (1986), Radiative forcing of the Venus mesosphere. 1. Solar fluxes and heating rates, *Icarus*, *67*(3), 484–514.

Cullen, M. J. P. (1993), The Unified Forecast/Climate Model, *Meteorol. Mag.*, *122*, 81–94.

Del Genio, A. D., and W. B. Rossow (1990), Planetary-scale waves and the cyclic nature of cloud top dynamics on Venus, *J. Atmos. Sci.*, *47*, 293–318.

Eliassen, A., and E. Palm (1961), On the transfer of energy in stationary mountain waves, *Geofys. Publ.*, *22*(3), 1–23.

Esposito, L. W., R. G. Knollenberg, M. Y. Marov, O. B. Toon, and R. P. Turco (1983), Clouds and hazes, in *Venus*, edited by D. M. Hunten et al., pp. 485-564, Univ. of Ariz. Press, Tucson.

Fels, S. B. (1977), Momentum and energy exchanges due to orographically scattered gravity waves, *J. Atmos. Sci.*, *34*(3), 499–514.

Fels, S. B., and R. S. Lindzen (1974), The interaction of thermally excited gravity waves with mean flows, *Geophys. Fluid. Dyn.*, *6*, 149–191.

Gierasch, P. J. (1975), Meridional circulation and the maintenance of the Venus atmospheric rotation, *J. Atmos. Sci.*, *32*, 1038–1044.

Hayashi, H., M. Shiotani, and J. C. Gille (2002), Horizontal wind disturbances induced by inertial instability in the equatorial middle atmosphere as seen in rocketsonde observations, *J. Geophys. Res.*, *107*(D14), 4228, doi:10.1029/2001JD000922.

Herrnstein, A., and T. E. Dowling (2007), Effects of topography on the spin-up of a Venus atmospheric model, *J. Geophys. Res.*, doi:10.1029/2006JE002804, in press.

Hide, R. (1969), Dynamics of the atmosphere of the major planets with an section on the viscous boundary layer at the rigid bounding surface of an electrically-conducting fluid in the presence of a magnetic field, *J. Atmos. Sci.*, *26*, 841–853.

Iga, S., and Y. Matsuda (2005), Shear instability in a shallow water model with implications for the Venus atmosphere, *J. Atmos. Sci.*, *62*, 2514–2527.

Imamura, T. (2006), Meridional propagation of planetary-scale waves in vertical shear: Implication for the Venus atmosphere, *J. Atmos. Sci.*, *63*(6), 1623–1636.

Kerzhanovich, V. V., D. Crisp, R. A. Preston, L. W. Esposito, A. P. Ingersoll, R. E. Young, J. E. Blamont, and V. V. Linkin (2003), Venus stratospheric

sounder: First in situ measurements in upper cloud region, *Acta Astronaut.*, *52*(2), 159–164.
Kliore, A. J., G. M. Keating, and V. I. Moroz (1992), Venus International Reference Atmosphere (1985), *Planet. Space Sci.*, *40*(4), 573.
Lebonnois, S., et al. (2006), Venus atmospheric dynamics from VIRTIS on Venus Express—Preliminary results, paper presented at 38th Division for Planetary Sciences Meeting, Am. Astron. Soc., Padasena, Calif.
Lee, C., S. R. Lewis, and P. L. Read (2006), A numerical model of the atmosphere of Venus, *Adv. Space Res.*, *36*(11), 2142–2145.
Lewis, S. R., and P. L. Read (2003), Equatorial jets in the dusty Martian atmosphere, *J. Geophys. Res.*, *108*(E4), 5034, doi:10.1029/2002JE001933.
Lindzen, R. S. (1990), *Dynamics in Atmospheric Physics*, Cambridge Univ. Press, New York.
Pedlosky, J. (1987), *Geophysical Fluid Dynamics*, Springer, New York.
Pollack, J. B., and R. E. Young (1975), Calculation of the radiative and dynamical state of the Venus atmosphere, *J. Atmos. Sci.*, *32*(6), 1025–1037.
Read, P. L. (1986), Super-rotation and diffusion of axial angular momentum: II. A review of quasi-axisymmetric models of planetary atmospheres, *Q. J. R. Meteorol. Soc.*, *112*, 253–272.
Read, P. L., and S. R. Lewis (2004), *The Martian Climate Revisited: Atmosphere and Environment of a Desert Planet*, Springer, New York.
Schneider, T. (2006), The general circulation of the atmosphere, *Annu. Rev. Earth Planet. Sci.*, *34*, 655–688.
Schubert, G. (1983), General circulation and the dynamical state of the Venus atmosphere, in *Venus*, edited by D. Hunten et al., pp. 681-765, Univ. of Ariz. Press, Tucson.
Seiff, A. (1983), Thermal structure of the atmosphere of Venus, in *Venus*, edited by D. Hunten et al., pp. 215-279, Univ. of Ariz. Press, Tucson.
Seiff, A., D. B. Kirk, R. E. Young, R. C. Blanchard, J. T. Findlay, G. M. Kelly, and S. C. Sommer (1980), Measurements of thermal structure and thermal contrasts in the atmosphere of Venus and related dynamics observations: Results from the four Pioneer Venus probes, *J. Geophys. Res.*, *85*, 7903–7933.
Taylor, F. W., D. M. Hunten, and L. V. Ksanfomaliti (1983), The thermal balance of the middle and upper atmosphere of Venus, in *Venus*, edited by D. Hunten et al., pp. 650-680, Univ. of Ariz. Press, Tucson.
Torrence, C., and G. P. Compo (1998), A practical guide to wavelet analysis, *Bull. Am. Meteorol. Soc.*, *79*, 61–78.
Walterscheid, R. L., G. Schubert, M. Newman, and A. J. Kliore (1985), Zonal winds and the angular momentum balance of Venus' atmosphere within and above the clouds, *J. Atmos. Sci.*, *42*(19), 1982–1990.
Yamamoto, M., and M. Takahashi (2003a), The fully developed superrotation simulated by a general circulation model of a Venus-like atmosphere, *J. Atmos. Sci.*, *60*, 561–574.
Yamamoto, M., and M. Takahashi (2003b), Superrotation and equatorial waves in a T21 Venus-like AGCM, *Geophys. Res. Lett.*, *30*(9), 1449, doi:10.1029/2003GL016924.
Zhu, X. (2006), Maintenance of equatorial superrotation in the atmospheres of Venus and Titan, *Planet. Space Sci.*, *54*, 761–773.

C. Lee, Division of Geological and Planetary Sciences, California Institute of Technology, M/C 150-21, Pasadena, CA 91125, USA. (lee@gps.caltech.edu)
S. R. Lewis, Department of Physics and Astronomy, Open University, Walton Hall, Milton Keynes MK7 6AA, UK.
P. L. Read, Department of Physics, University of Oxford, Oxford OX1 3PU, UK.